

Review of Incompressible, Turbulent Bluff-Body Wake Analysis and Modeling Techniques

Logan D. Halstrom* and Federico Zabaleta†
University of California, Davis, California, 95616

abstract here **LH&FZ**

Each full-length paper must have a summary-type abstract of 100 to 200 (maximum) words in one paragraph, without numerical references, acronyms, or abbreviations. The abstract indicates the subjects dealt with in the paper and states the objectives of the investigation.

Nomenclature

α	=	Angle of attack, deg
ρ	=	Density, kg/m^3
Re	=	Reynolds Number, N.D.
C_d	=	2-Dimensional drag coefficient, N.D.
∇	=	Gradient function
V	=	Velocity, m/s
u	=	Einstein notation velocity, m/s
x	=	Einstein notation dimension, m
P	=	Pressure, Pa
μ	=	Dynamic viscosity, $Pa \cdot s$
t	=	Time, s

Subscripts

$(\cdot)_\infty$	=	Freestream quantity
$(\vec{\cdot})$	=	Vector quantity
$(\bar{\cdot})$	=	Mean quantity (time-averaged)
$(\cdot)'$	=	Perturbation quantity
$(\cdot)_D$	=	Diameter as reference length
$(\cdot)_i$	=	Einstein notation index
$(\cdot)_j$	=	Einstein notation index

*Graduate Student, Mechanical And Aerospace Engineering Department, One Shields Avenue

†Graduate Student, Civil and Environmental Engineering Department, One Shields Avenue

I. Introduction

WHEN a body moves in a fluid, it experiences two types of forces: shear force due to friction and normal force due to pressure. Integration of the distribution of these forces along the surface of the body results in an overall force vector on the body, which can be expressed in components such as the familiar combination of lift and drag. The drag force can be thought of as a summation of the net surface shear and net surface pressure difference in the direction of the body's velocity.

The shear drag, commonly called friction drag, occurs due to a difference in velocity in the surface of the body and the mean flow. This friction is associated with the development of boundary layers and is it scales with the Reynolds number. Alternatively, the drag due to pressure differences along the surface of the body is called pressure drag or viscous induced pressure drag, as this drag is usually associated with separation of the flow and the formation of a wake downstream the body. In real flows, drag is composed by the combination of both. The contribution of friction drag is usually dominant in attached flows while the pressure drag prevails in separated flows.

The differences between friction and pressure drag can be illustrated by considering the flow around a flat plate. If the flat plate is oriented in the direction of the flow, then the boundary layer will remain attached and friction drag will dominate while the pressure drag will be almost negligible. Conversely, if the flat plate is oriented perpendicularly to the flow, the boundary layer will separate at the edges and the low pressure in the separated, aft region will create a difference in pressure between both sides of the plate. This net pressure drag will be much more significant than the friction drag acting in the minuscule regions of attached boundary layer.

These definitions of drag are necessary to define the concept of a bluff-body (equivalently known as a blunt-body), which is a fundamental, generic body shape in aerodynamics and the central concept discussed in this paper. A bluff-body is defined as a body where the major contribution to total drag is pressure drag, as in the case of the perpendicular flat plate [1]. Conversely, the drag of a streamlined body will be composed primarily of friction drag, as in the case of the streamwise-oriented plate.

An illustration of the differences in shape and flow behavior between these two body shapes can be found in Fig 1. From the figure, the origin of the streamlined body's name is obvious: The streamlines of the surrounding flow follow the shape of the body smoothly, which indicates that the boundary layer is attached and the dominant form of drag is from friction. Above the streamlined airfoil, flow over a square cylinder is shown to demonstrate the stark differences of bluff-body flow. Other examples of bluff-bodies include circular cylinders, cubes, spheres, and airfoils at large angle of attack. The flow for all of these bluff-bodies can be characterized by the four common flow features annotated in Fig 1: an attached boundary layer (minimal for the square), a separated shear layer that may or may not reattach, a recirculation zone behind the blunt face of the bluff-body where flow is entrained after which it coalesces into a coherent wake [2].

For the sake of terminology commonly found in the literature pertaining to bluff-bodies, it is also relevant to define the concept of base pressure [3]. Because the flow over bluff-bodies is characterized by massive separation and a detached shear layer, it follows that there will be no pressure recovery along the surface of the body in the separated region. Thus, the surface pressure along the aft of a bluff-body remains at a nearly constant value, which is commonly described as a “base pressure”. This base pressure value is lower than that which would be found in an equivalent but non-physical “inviscid” flow, as is illustrated by Frank White in the right of Fig 1, where attached flow would allow the pressure to rise again to stagnation values at the back of the sphere. Base pressure is thus the primary contributor to the dominating pressure drag of the bluff-body. It is also important to note that bluff-body flows may be called “base flows” in reference to the base pressure.

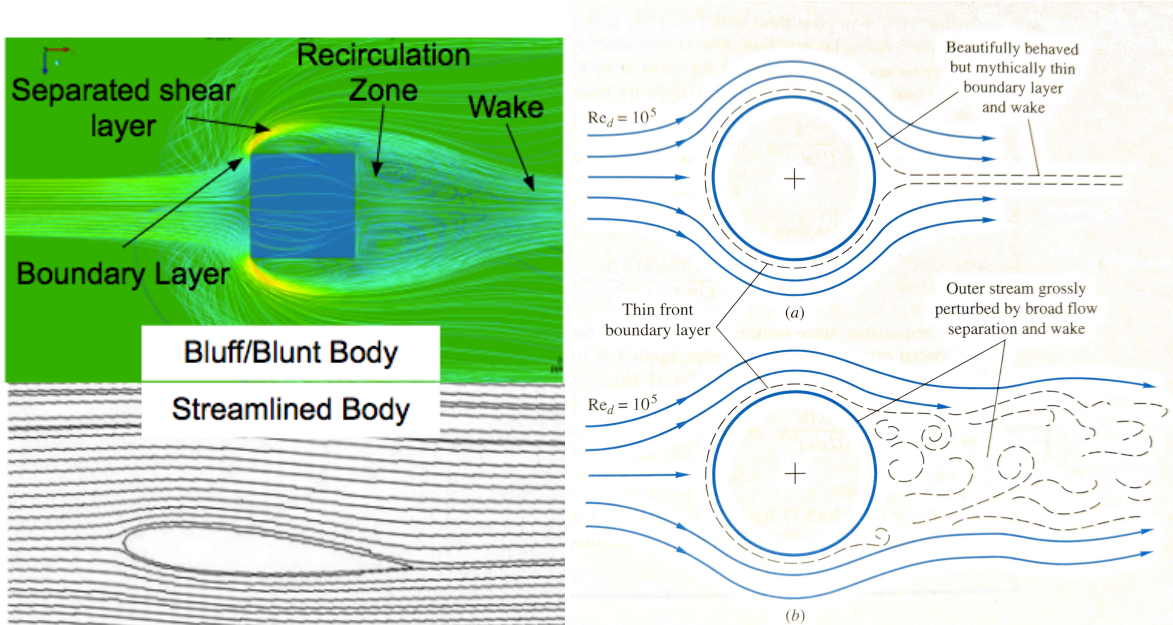


Fig. 1 Demonstration of the flow differences between a bluff-body with massive separation [4] and a streamlined body with primarily attached flow (left) and illustration of non-physical, inviscid flow over a bluff-body with no separation and realistic, viscous flow with massive separation (right) [5]

Bluff-body flow is applicable to a plethora of real-world applications. Massively separated wakes are characterized by complex, unsteady, and sometime unstable turbulent phenomena, which can lead to design concerns throughout the fields of engineering. A few examples of bluff-body flow in engineering applications include wall-mounted cubes representative of a high-rise buildings [2], bridge spans [6] as modeled in Fig 2, ground vehicles [7] like the passenger sedan shown in Fig 4, atmospheric reentry vehicles [8] like the Orion wind tunnel model in Fig 3, humans in ejection seats and parachutes, both demonstrated in Fig 3, aircraft protuberances such as landing-gear trucks, space launch vehicles, and flame holders [9] in combustors Fig 5.

Bluff-bodies are common in civil engineering applications, where engineers might be concerned in predicting

unsteady wind loading leading to structural resonance, which was a major design flaw for the Tacoma Narrows Bridge. Fig 2 demonstrates a model bridge span undergoing wake-induced vibration due to the vortex shedding caused by the gap in the center [6].

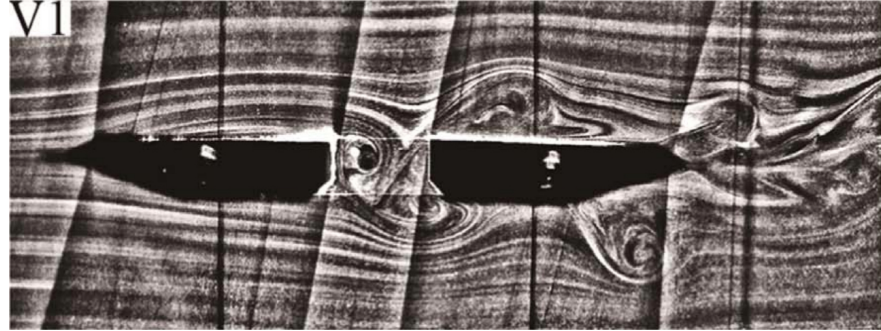


Fig. 2 Instantaneous PIV flow field of bridge model similar to Tacoma Narrows bridge ($Re=587$) [6]

Unsteady loading and buffeting can also be a potentially catastrophic bluff-body wake effect for mechanical and aerospace engineering applications. The dynamic situation of a cockpit emergency egress system as depicted in Fig 3 requires precise understanding of the unsteady forces on the ejection seat and human in order to mitigate any injuries the escaping pilot might experience.



Fig. 3 Left: Mk-16 ejection seat rocket sled test (Martin-Baker), Right: Shadowgraph wake of Orion capsule model ($M = 0.3, \alpha = 29.25^\circ, Re_D = 5.3 \times 10^6$) [8]

Dynamic stability can also be adversely affected by bluff-body wake behavior. The drogue parachute in Fig 3 and the model Orion capsule in Fig 3 are both situations where dynamic instability of the bluff-body could lead to potentially fatal situations for the humans involved.

Acoustics can also be a design concern either due to unsteady loading as in the case of a launch vehicle or due to noise concerns or restrictions such as those for aircraft noise. Even passenger vehicles such as that shown in Fig 4 can create a separated wake which could lead to acoustic disturbance of the passengers inside.

There are even applications for bluff-bodies outside the concepts of loading and acoustics. In industrial applications



Fig. 4 Streamlines and separated flow over a car in a wind tunnel (NASA/Eric James)

where a high-speed mixture must be ignited, it is necessary to both reduce the speed and mix the flow around an ignition source to allow a flame to stabilize. This effect can be created by placing a triangular bluff-body directly upstream of an ignitor such that its recirculation region entrains slower-moving mixture at the ignitor's location (Fig 5) [10].

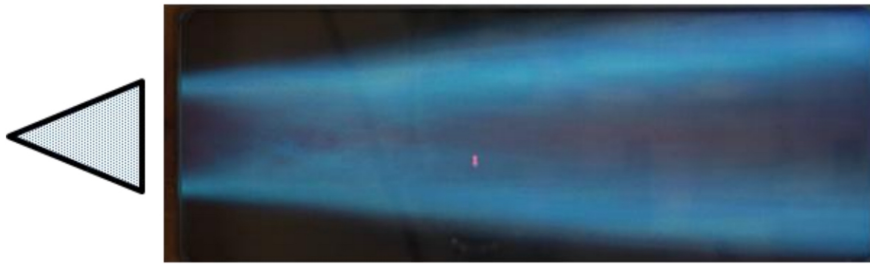


Fig. 5 Image of a stabilized flame held in the wake of a bluff-body flame holder [9]

The wakes of bluff-bodies are extremely complex, containing many scales of turbulent structures and can be highly unstable. These facts simultaneously impress upon the importance of understanding the effects of bluff-body flows for engineering applications and gives rise to long-term difficulties in modeling and observing bluff-body flow. The study presented in this article will attempt to connect the entire field of bluff-body fluid dynamics, archiving the fundamental concepts and historical approaches, assessing modern techniques of experimental and computational analysis, and discussing the challenges that remain.

II. Flow around a bluff body and transition

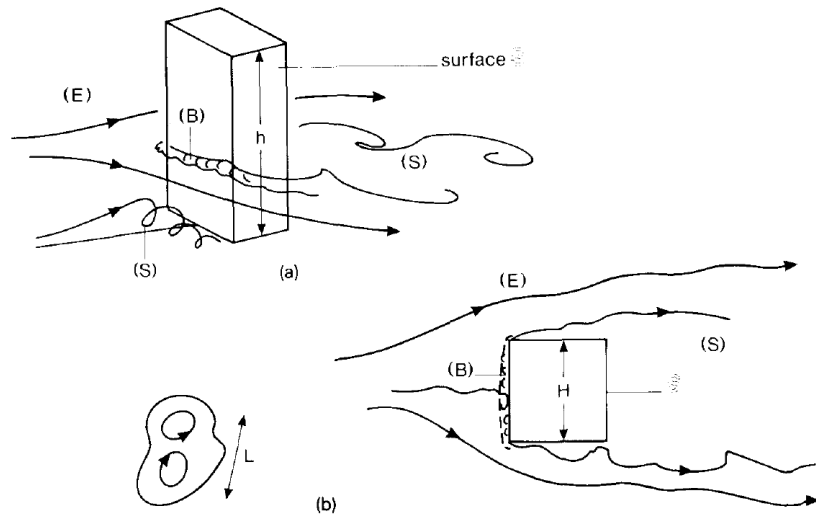


Fig. 6 Regions of disturbed flow. Extracted from [11]

A. Steady laminar wake

B. Periodic Laminar Regime

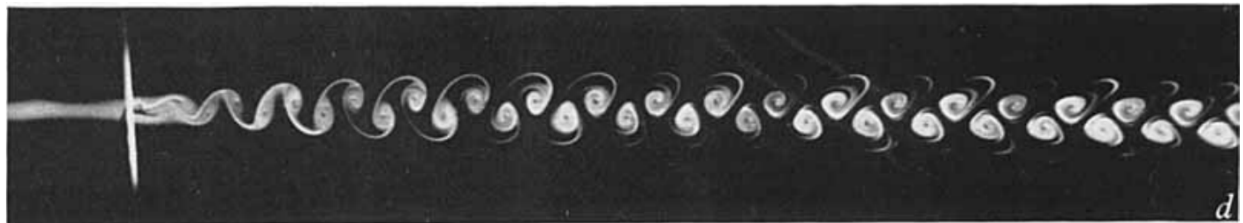


Fig. 7 Kármán-Bénard eddy street at $Re = 100$. Extracted from [12]

C. Transition in wake state



Fig. 8 Transition in wake at $Re = 190$. Extracted from [12]

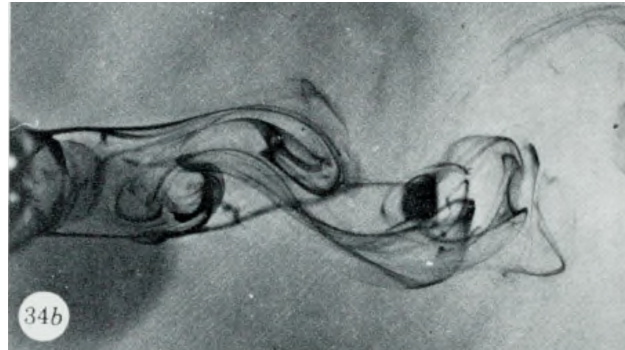


Fig. 9 Transition in wake at $Re = 344$. Extracted from [13]

D. Transition in shear layers state

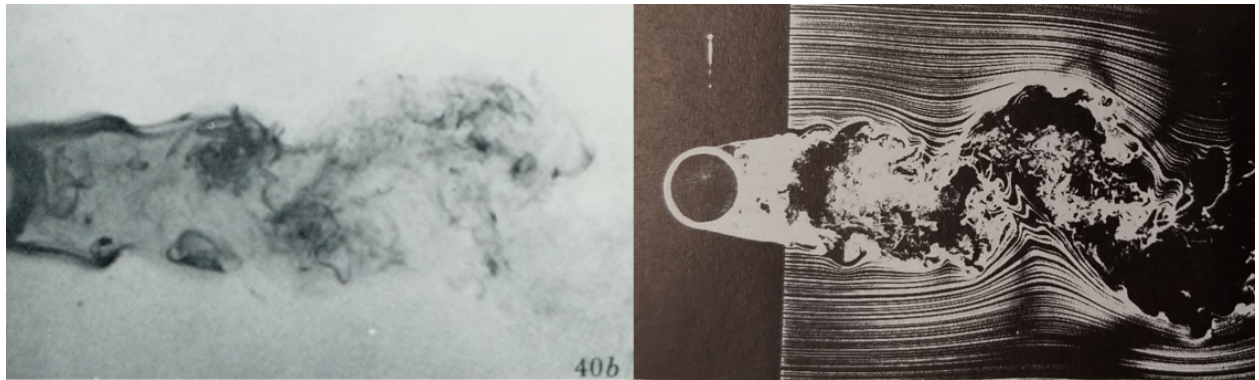


Fig. 10 Transition in free shear layer. Left: $Re = 1083$. Extracted from [13]. Right: $Re = 8000$. Extracted from [14]

E. Transition in boundary layer

F. Fully turbulent state

III. Free stream turbulence and non-uniform free stream

IV. Experimental Methods And Results

FZ

- Historical Study
- Experimental techniques
 - ballistic range?
- Applications
 - Simple cases: cylinder/sphere

- * Drag vs Re?
- * Wake velocity profiles?
- * Wake structure?
- Sharp vs bluff: sphere vs cube
- Complex cases: capsule/building

V. Computational Methods and Results

Due to the highly complex nature of bluff-body wake separation and behavior, the primary realistic method of simulation for these flows is discrete solution of the Navier-Stokes equations (Eqn 1) or Computational Fluid Dynamics (CFD). Analytic, inviscid formulations such as potential flow methods yield the non-physical results depicted in the top image of Fig 1, where there is separation or corresponding base pressure, making this fictional flow a non-bluff-body. The same deficiencies apply to numeric, inviscid formulations, such as panel method or Euler's equation. Within the field of CFD, there is a diverse set of techniques for handling the simulation of turbulence, and the detailed description of each of these is beyond the scope of this study. Instead, the key concept of each method relevant to bluff-body flow will be listed here to provide the basis for the comparisons to follow.

A. Turbulence Modeling Overview

Discrete solution of the full Navier-Stokes equations is referred to as Direct Numeric Simulation (DNS). The incompressible form of the continuity and momentum equations for this formulation are provided in Eqn 1. No turbulence modeling is required for this simulation, so results will be as realistic as the domain discretization and continuum, Newtonian fluid constraints allow. The disadvantage of DNS lies in the requirement that all scales of turbulence must be resolved within the domain to achieve realistic results, which makes simulation of the majority of flows infeasible with the current state of computational technology.

$$\begin{aligned} \vec{\nabla} \vec{V} &= 0 \\ \rho \frac{D\vec{V}}{Dt} &= \rho \vec{g} - \vec{\nabla} P + \mu \vec{\nabla}^2 \vec{V} \end{aligned} \tag{1}$$

The Navier-Stokes equations can be reduced to a form that is solvable by todays standards by separating them in to mean and fluctuation components via the process of Reynolds decomposition. This results in the Reynolds-Average Navier-Stokes (RANS) equations of which the incompressible momentum equation is provided for example in Eqn 2.

$$\rho \frac{D\bar{\vec{V}}}{Dt} = \rho \vec{g} - \vec{\nabla} \bar{P} + \mu \vec{\nabla}^2 \bar{\vec{V}} - \rho \frac{\partial}{\partial x_j} (\bar{u'_i} \bar{u'_j}) \tag{2}$$

where the overbar represents the time average and the vertical tick represents a perturbation quantity. Unfortunately, the infamous turbulence closure problem requires that some relation must be derived for the additional unknown “Reynolds stress” term $\rho \overline{u'_i u'_j}$. Turbulence models allow the estimation of this term and the closure of the RANS equations to notable success, but inherent inaccuracy is introduced by the nature of modeling.

A slight variation of RANS is Unsteady RANS (URANS), which is a time-accurate method that requires all grid cells to be fixed to the same global time step. This allows URANS to capture unsteady behavior of the mean flow.

In recent years, the advantages of DNS in resolving fine turbulent behavior have been brought into use through the compromising strategy of Large Eddy Simulation (LES), where turbulent structures that are large enough to be resolved on the chosen computational grid are solved with DNS, and smaller turbulent scales are solved with a turbulence model called a Subgrid-Scale (SGS) model. This methodology results in much higher fidelity turbulence spectra and unsteady behavior but comes at the cost of more computational time required.

This method was enhanced by Spalart to operate with RANS as the Subgrid Scale Model, effectively combining the two methods into a hybrid RANS/LES method coined Detached Eddy Simulation (DES) [15].

Finally, Scale Adaptive Simulation (SAS) is a RANS-like method developed by Menter [16] that uses a dynamic von Karman length-scale in its turbulence model, which allows the resolution of the full turbulent spectrum and results in LES-like results.

B. Simulation Comparisons: Simple Geometry

LES = DES

discuss RANS vs DES cost

discuss RANS vs DES accuracy

DES choice of RANS model important for determining separation

The fundamental differences between the CFD methodologies previously described in Section V.A can result in noticeable variations in simulation results; especially for massively separated wakes. A first look at these differences is offered in Fig 11, which is a comparison of flow over a circular cylinder calculated using various RANS and DES methods from Spalart and Travin [15] and comparable SAS cases from Menter [16]. The circular cylinder is arguably the simplest bluff-body shape and therefore offers a relatively unbiased platform upon which to compare these different solvers.

In this instance, we are observing simulations for a diameter-based Reynolds number of $Re_D = 5 \times 10^4$, which corresponds to laminar separation, and we are comparing the time-averaged result for drag coefficient C_d from each simulation to the range of instantaneous $C_d = 1.15 - 1.25$ observed in experiment at a similar Reynolds number [17].

The simplest of all of these models is the steady RANS case (a), where the wake vorticity isocontours demonstrate that only the two-dimensional separated shear layer is predicted. This very low-fidelity wake results in a correspondingly

inaccurate C_d compared to the wind tunnel range. RANS simulations can be significantly improved, however, by modeling time-accurate changes in the mean and allowing three-dimensional flow effects to develop, as is the case for 3D URANS. In this simulation, the flow is significantly more realistic than steady RANS, though much of the three-dimensionality is still suppressed [15]. Averaging and integration of this wake behavior results in a C_d that is just within the upper range of the wind tunnel values, which is a significant improvement upon steady RANS.

Even higher-fidelity results may be obtained from LES-based methods such as DES, for which three cases are shown in Fig 11. For all three cases, it is obvious that the application of DNS to the larger turbulence scales results in a more three-dimensional and life-like simulation of turbulent wake effects. This improvement in modeling can be useful for engineering design cases that require unsteady loading or acoustic profile data. The time-averaged C_d values for each DES case, however, remain on the fringes of the experimental range, suggesting that the increased computational cost of DES may not always be compensated for by higher accuracy in time-averaged results. Still, it is important to note that these comparisons are highly dependent on the method and window of averaging and a single metric such as C_d is insufficient on its own to determine the superiority of a CFD method [17].

The three DES results can also be used to illustrate uncertainties in the method due to discretization and turbulence modeling. The DES-SA (Spalart-Allmaras) cases demonstrate that grid refinement in the LES-regions allows resolution of fine turbulent scales and can significantly alter the time-averaged results. The comparison of the SA and Shear-Stress Transport (SST) RANS models demonstrates that the choice of RANS model has little effect on the LES-regions of the DES solution, but can noticeably influence the separation prediction in the RANS-regions.

Lastly,

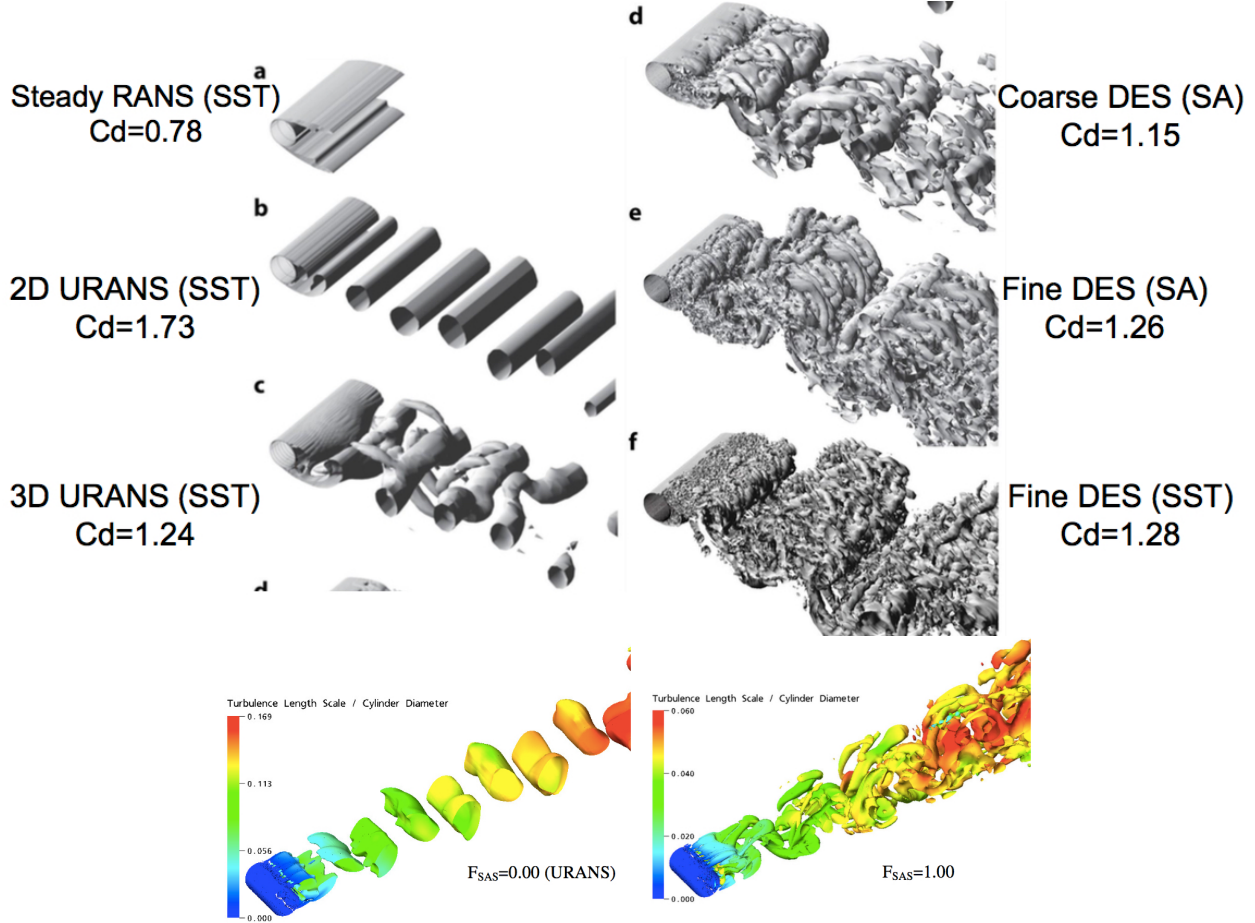


Fig. 11 Comparison of wind tunnel test of a circular cylinder with drag fluctuating coefficient ranging from $C_d = 1.15 - 1.25$ compared with time-averaged C_d values from simulations using RANS (a), 2D URANS (b), 3D URANS (c), DES-SA on a coarse grid (d), DES-SA on a fine grid (f), and DES-SST on a fine grid (e) [15] in black and white and SAS simulations with null (left) and finite (right) adjustable length-scales in color [16]. Visualizations are isocontours of vorticity

Vorticity isosurfaces by a circular cylinder: $ReD = 5 \times 10^4$, laminar separation. Experimental drag coefficient $C_d = 1.15-1.25$. (a) Shear-stress transport (SST) turbulence model steady Reynolds-averaged Navier-Stokes (RANS), $C_d = 0.78$; (b) SST 2D unsteady RANS, $C_d = 1.73$; (c) SST 3D unsteady RANS, $C_d = 1.24$; (d) Spalart-Allmaras (SA) detached-eddy simulation (DES), coarse grid, $C_d = 1.16$; (e) SA DES, fine grid, $C_d = 1.26$; (f) SST DES, fine grid, $C_d = 1.28$. Figure courtesy of A. Travin

illustrates the response of DES to grid refinement in its LES region.

DES solutions with different base RANS models are not sensitive to model choice in the LES region (as opposed to the RANS region, particularly if separation occurs).

SAS cylinder: Resolved structures for cylinder in crossflow using different constants $FSAS = 3.6e6$

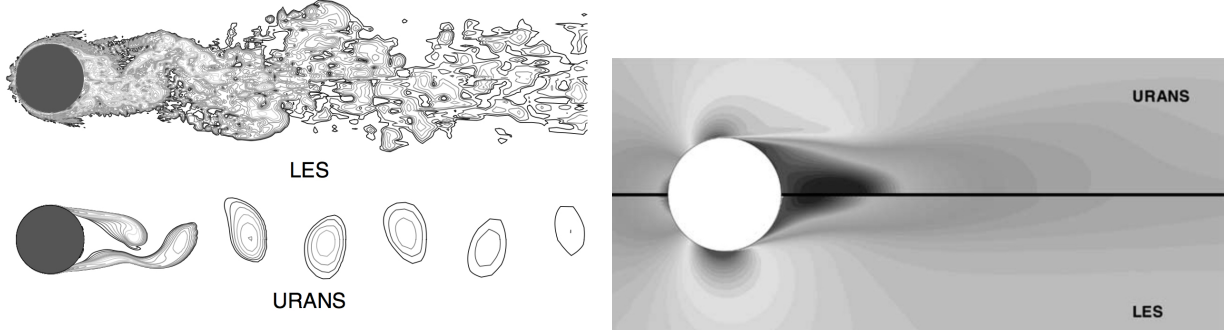


Fig. 12 cylinder les vs urans instantaneous and averaged [18]

Instantaneous vorticity magnitude at a given spanwise cut for flow over a circular cylinder at $Re_D = 1/4 1 106$. 25 contour levels from $x/D = U_1/4 1$ to $x/D = U_1/4 575$ (exponential distribution) are plotted.

Fig. 5. Mean streamwise velocity distribution predicted by LES and URANS. 45 contour levels from $U = U_1/4 0:2$ to $U = U_1/4 1:7$ are plotted.

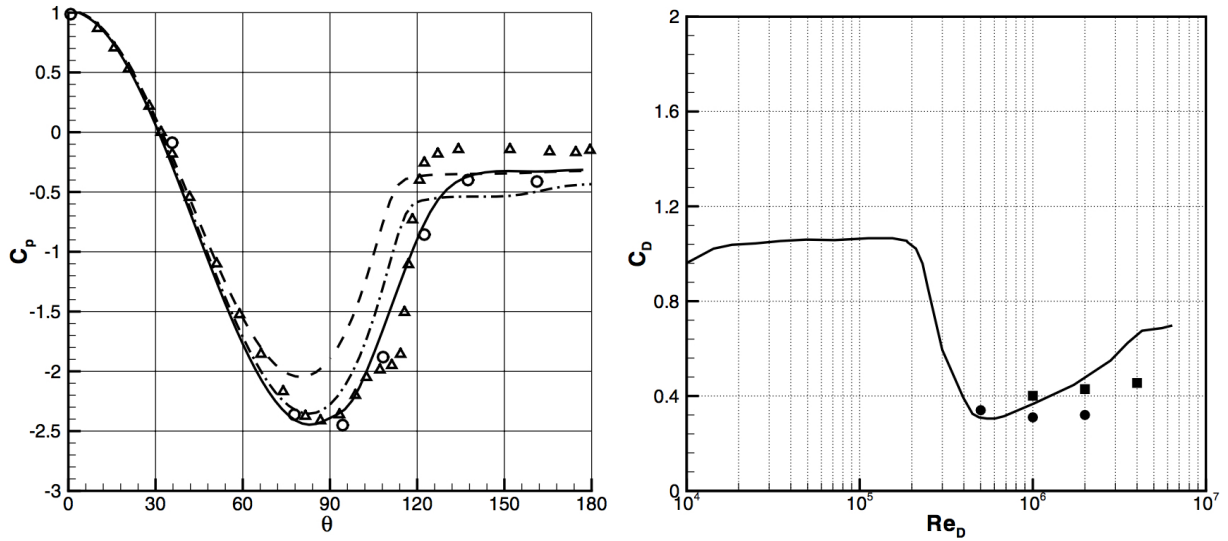


Fig. 13 rans vs les [18]

Mean pressure distribution on the cylinder: (—) LES at $Re_D = 1/4 1 106$; (---) RANS at $Re_D = 1/4 1 106$; (-.-) URANS at $Re_D = 1/4 1 106$; (o) experiment by Warschauer and Leene (1971) at $Re_D = 1/4 1:2 106$ (spanwise averaged); (Δ) experiment by Falchsbart (in Zdravko-vich, 1997) at $Re_D = 1/4 6:7 105$.

Drag coefficient as a function of the Reynolds number. (—) Achenbach (1968); (circle) LES; (square) URANS.

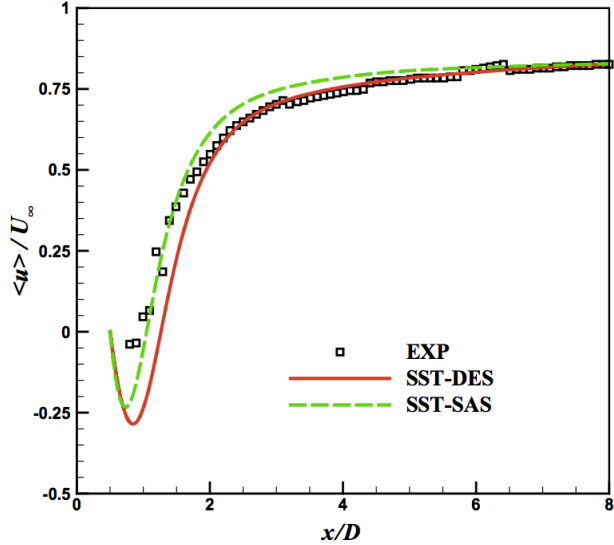
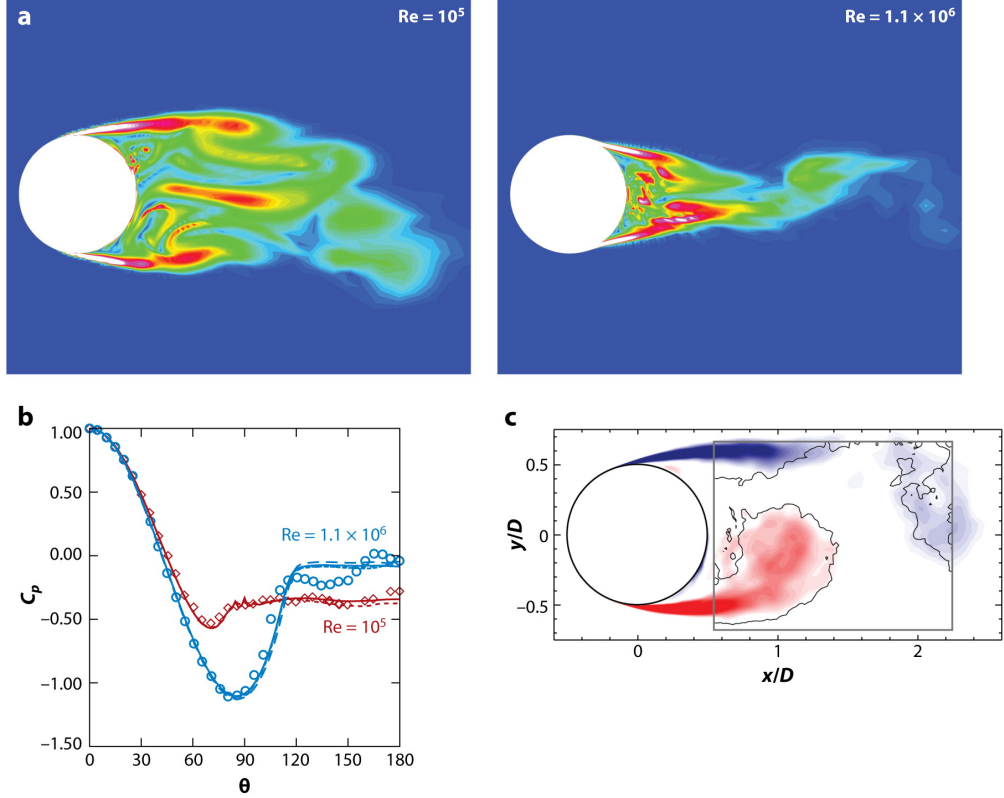


Fig. 14 cylinder des vs sas time-averaged wake velocity [19]

$Re_D = 1.4 \times 10^5$, same grid for both solvers, SAS shows good agreement in mean flow properties of near wake, convergence of both solvers in far wake. SAS can have some advantages at same computational cost, SAS is more dissipative,

Preliminary study, Slipstream analysis of high-speed train, DDES was most like experiment but SAS was comparable. Independent grid and time step refinement.

computational cost: URANS:SAS:DDES = 1:10:20 [20]



A Spalart PR. 2009.
R Annu. Rev. Fluid Mech. 41:181–202

Fig. 15 DES validation from [15]. Sphere transition and drag crisis from [21]. Vorticity validation from [22]

Simple bluff bodies. (a) Flow visualizations and (b) pressure distributions for a sphere. $Re = 10^5$ and 1.1×10^6 . Open circles and diamonds denote experiments, whereas the dotted and dashed lines denote detached-eddy simulation (DES) on two grids. Panels a and b courtesy of K. Squires. (c) Phase-averaged vorticity contours for a cylinder. Color gradations denote DES conducted by Mockett et al. (2008), and the solid line denotes experiments by the same authors.

NOTE: DES could be used to emulate the dimples on a golf ball by setting the boundary layer separation point, but true simulation of flow in golf ball dimples requires DNS due to the range of scales

C. Simulation Comparisons: Complex Geometry

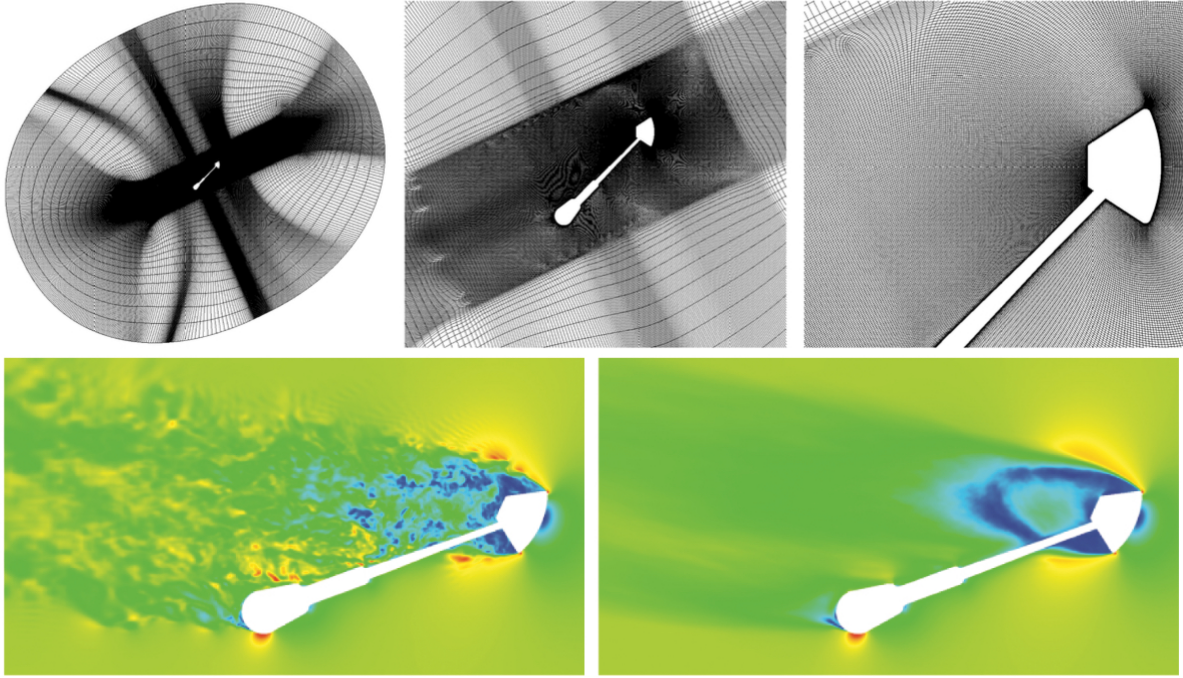


Fig. 16 Orion capsule grid and Mach number instantaneous (left) time-averaged (right) (DES, M=0.5) [23]

Plots of Mach number for an instantaneous and time-averaged solution. For an illustration of the amount of unsteadiness this removed, refer to Fig. 6. It shows a slice of Mach number through the pitch plane ($\phi = 0$ deg) for a DES–KEC solution at Mach 0.50, AoA 170 deg.

RANS did ok compared to WTT/DES for some cases but in others, DES outperformed

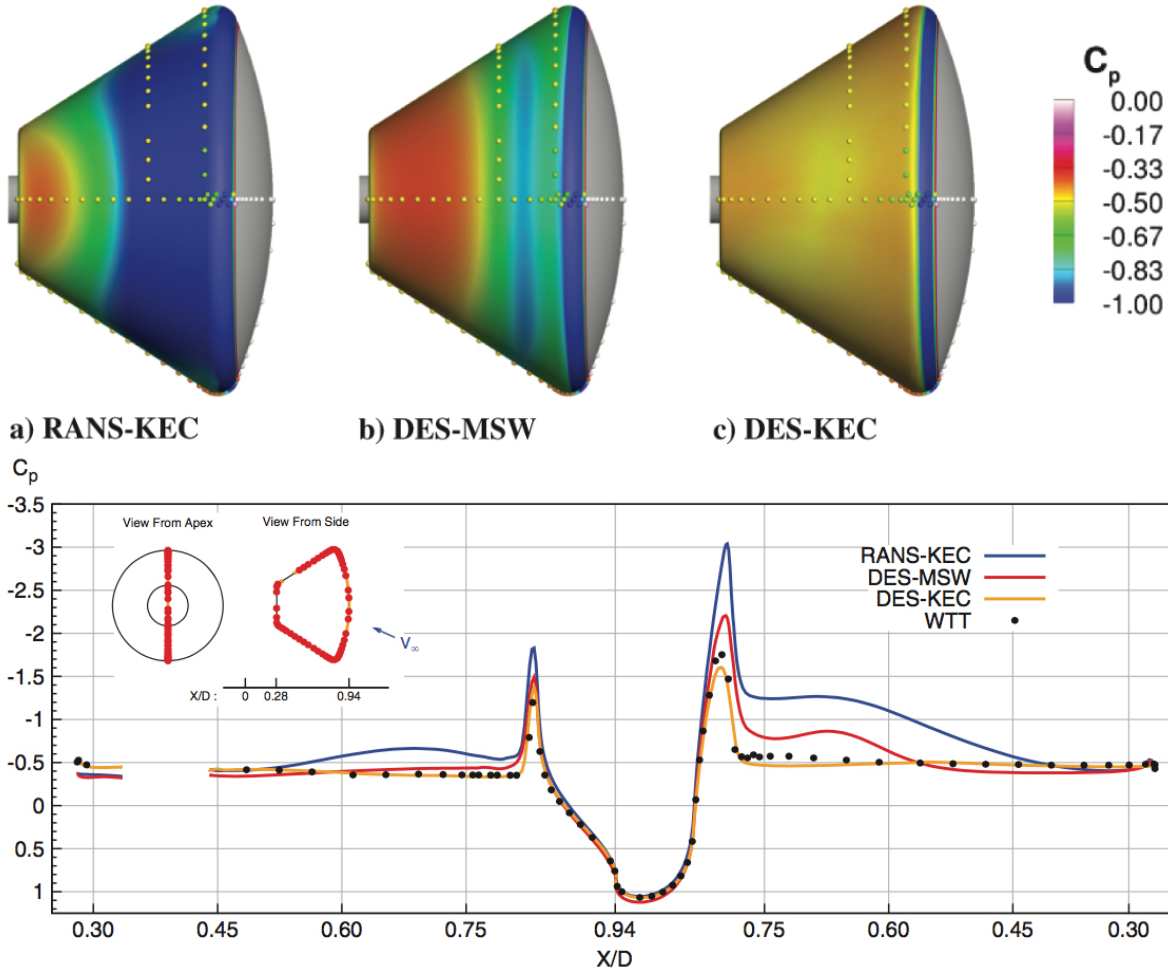


Fig. 17 surface pressure and pressure tap comparison of RANS, DES, WTT, M=0.5 [23]

Freckle plots of pressure tap data, viewed from fi 180 deg, for Mach 0.50, AoA 155 deg case

Line plots of pressure tap for data Mach 0.50, AoA 155 deg case.

RANS fails to predict suction peak, surface pressures in wake. Gets best lift integration compared to DES due to separation prediction, worse drag due to wake pressure prediction.

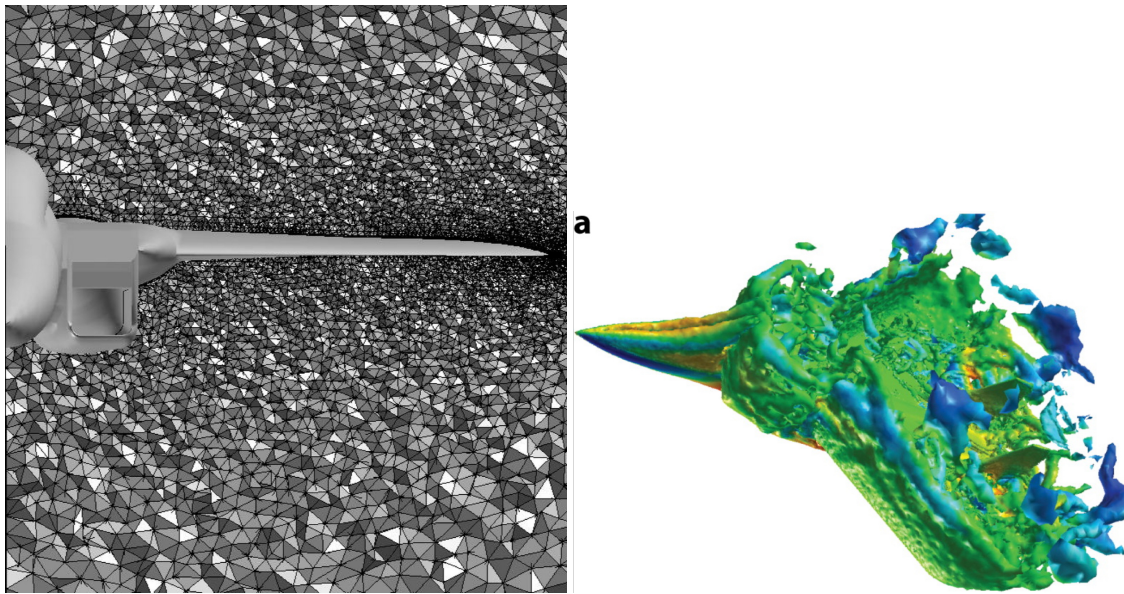


Fig. 18 F-15 DES grid (left) [24] vorticity isocontours (right) [15]

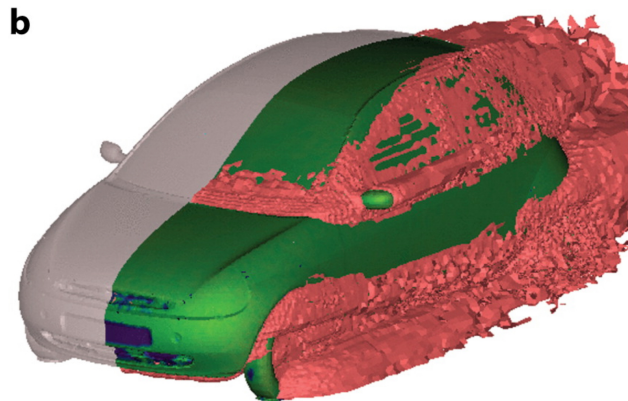


Fig. 19 car DES isocontours [7]

VI. Current State of Bluff-Body Turbulence Analysis

- Current State of Knowledge
- Remaining Challenges

A. Experimental Methods

FZ

B. Computational Methods

- Current State of Knowledge

- Remaining Challenges
- des GIS and order of accuracy

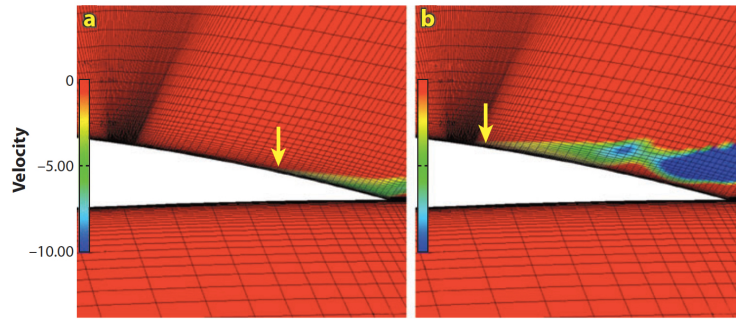


Fig. 20 Example of DES grid induced separation from [15], source: [25]

Vorticity contours over an airfoil: (a) Reynolds-averaged Navier-Stokes and (b) detached-eddy simulation. Arrows indicate separation. Figure taken from Menter & Kuntz 2002.

Potential con of using DES. EXPLAIN HOW GRID INDUCED SEPARATION WORKS.

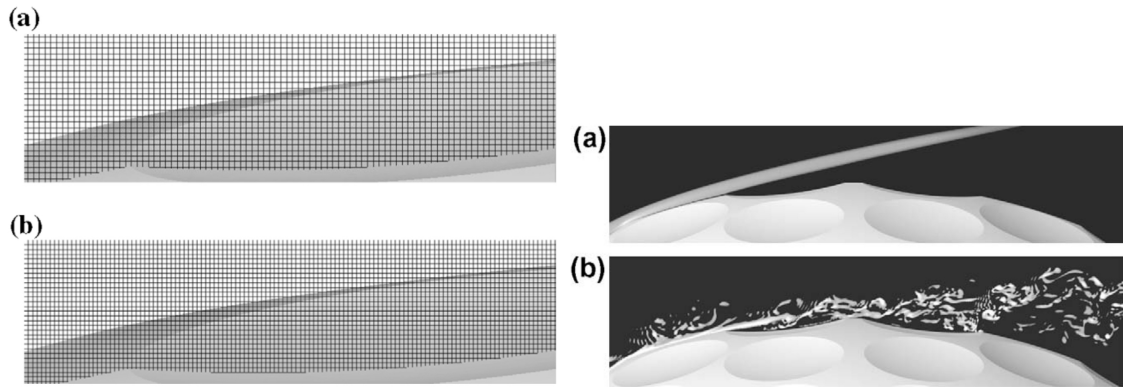


Fig. 21 DNS non-rotating golf ball with dimples grid (left) vorticity (right) [26]

Example grid resolution in a dimple near 84° (measured from the stagnation point at the front of the golf ball). (a) $Re = 2.5 \cdot 10^4$; (b) $Re = 1.1 \cdot 10^5$.

Contours of azimuthal vorticity. (a) $Re = 2.5 \cdot 10^4$; (b) $Re = 1.1 \cdot 10^5$

NOTE: Recall sphere example from Spalart review and say that this is the analogous DNS experiment to his DES

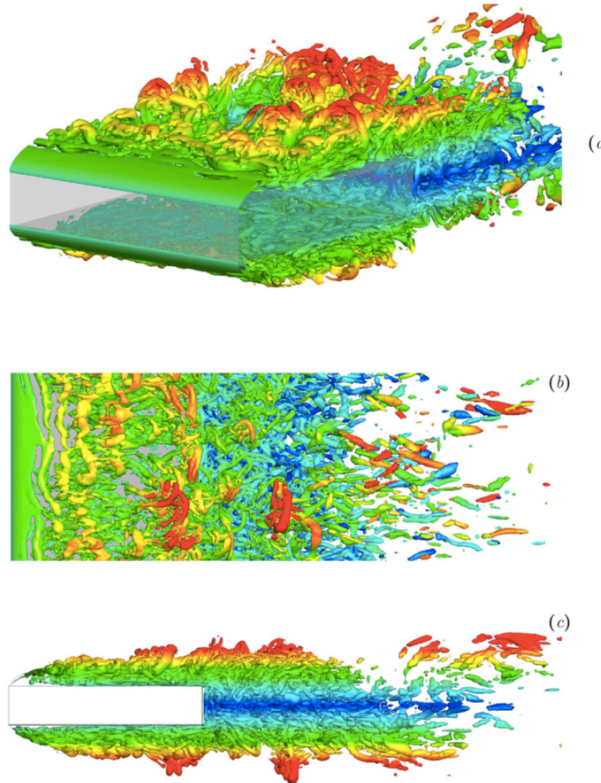


Fig. 22 DNS square cylinder vorticity contours Re=3000 [27]

Fig. 10. Instantaneous isosurfaces of $\lambda_2 = -2$ colored with y . Perspective, top and lateral views in (a), (b) and (c) plots, respectively.

LH

- Brief turbulence model description
 - RANS vs URANS
 - DNS
 - LES (uses DNS) and DES (=Hybrid RANS/LES)
- Compare turbulence model performance for sphere/cylinder
 - DES > URANS > RANS
 - DES = functional LES
 - SAS vs DES?
 - DNS: limited Re
- Shortcomings of each model (and how to address them)
 - URANS
 - DES: only good at sharp separation

- * “An order of accuracy has not even been proposed for a simulation using both modes within DES”
 - Spalart about hybrid method
- * grid induced separation (maybe not an issue for bluff bodies)
- * DES can default to RANS if grid adaptation misses a shear layer
- * more computational cost than RANS
- Advanced geometries
 - f-15
 - car
 - building
 - capsule
 - chute, landing gear, helicopter, wind turbine

LIST ALL FIGURES HERE, REORDER AND DESCRIBE LATER

VII. Conclusions

LH&FZ

Conclusions provide a detailed discussion of study findings. Do not introduce concepts not presented in text; do not refer to other work.

Acknowledgments

LH&FZ

Example citations

[28]

References

- [1] Anderson Jr, J. D., *Fundamentals of aerodynamics*, McGraw-Hill, New York, NY, USA, 2010.
- [2] Elkhoury, M., “Assessment of turbulence models for the simulation of turbulent flows past bluff bodies,” *Journal of Wind Engineering and Industrial Aerodynamics*, Vol. 154, 2016, pp. 10 – 20. doi:<https://doi.org/10.1016/j.jweia.2016.03.011>, URL <http://www.sciencedirect.com/science/article/pii/S0167610515300945>.
- [3] Tanner, M., “Theories for base pressure inincompressible steady base flow,” *Progress in aerospace sciences*, Vol. 34, No. 7-8, 1998, pp. 423–480.
- [4] Richards, P., and Norris, S., “LES modelling of unsteady flow around the Silsoe cube,” *Journal of Wind Engineering and Industrial Aerodynamics*, Vol. 144, 2015, pp. 70–78.

- [5] White, F. M., *Fluid Mechanics*, 2011, McGraw-Hill, New York, NY, USA, 2011.
- [6] Yuan, W., Laima, S., Chen, W., Li, H., and Hu, H., “Investigation on the vortex-and-wake-induced vibration of a separated-box bridge girder,” *Journal of Fluids and Structures*, Vol. 70, 2017, pp. 145 – 161. doi:<https://doi.org/10.1016/j.jfluidstructs.2017.01.015>, URL <http://www.sciencedirect.com/science/article/pii/S0889974616304911>.
- [7] Mendonça, F., Allen, R., de Charentenay, J., and Lewis, M., “Towards Understanding LES and DES for Industrial Aeroacoustic Predictions,” *International workshop on ‘LES for Acoustics’*, DLR Göttingen, Germany, October 2002.
- [8] Ross, J. C., Heineck, J. T., Burnside, N., Sellers, M. E., Halcomb, N., Garbeff, T., Yamauchi, G., and Kushner, L., “Comprehensive Study of the Flow Around a Simplified Orion Capsule Model,” *31st AIAA Applied Aerodynamics Conference*, San Diego, CA, June 2013.
- [9] Tanaka, S., Takahashi, K., Hosoi, J., and Uchida, M., “Bluff Body Flame Holder with Flow Entrainment Using Perforated Plate,” *9th AIAA/ASME/SAE/ASEE Joint Propulsion Conference*, San Jose, CA, July 2013.
- [10] Li, H., Sung, H., and Yang, V., “Large Eddy Simulation of Combustion Dynamics of Bluff Body Stabilized Flame,” *49th AIAA Aerospace Sciences Meeting including the New Horizons Forum and Aerospace Exposition*, Orlando, Florida, January 2011.
- [11] Hunt, J., Kawai, H., Ramsey, S., Pedrizetti, G., and Perkins, R., “A review of velocity and pressure fluctuations in turbulent flows around bluff bodies,” *Journal of Wind Engineering and Industrial Aerodynamics*, Vol. 35, 1990, pp. 49 – 85. doi:[https://doi.org/10.1016/0167-6105\(90\)90210-4](https://doi.org/10.1016/0167-6105(90)90210-4), URL <http://www.sciencedirect.com/science/article/pii/0167610590902104>.
- [12] Zdravkovich, M., “Smoke obervations of the formation of a Kárman vortex street,” *Journal of Fluid Mechanics*, Vol. 37, No. 3, 1968, pp. 491 – 496. doi:[doi:10.1017/S0022112069000681](https://doi.org/10.1017/S0022112069000681), URL <https://www.cambridge.org/core/journals/journal-of-fluid-mechanics/article/smoke-observations-of-the-formation-of-a-karman-vortex-street/C9BFB26B8A755EAFFFA6ACC3C91800FB>.
- [13] Gerrard, J. H., “The wakes of cylindrical bluff bodies at low Reynolds number,” *Philosophical transactions of the Royal Society A*, Vol. 288, 1978, pp. 351 – 382. doi:<https://doi.org/10.1098/rsta.1978.0020>, URL <http://rsta.royalsocietypublishing.org/content/288/1354/351.article-info>.
- [14] Zdravkovich, M. M., “Flow around Circular Cylinders; Volume 1. Fundamentals,” *Journal of Fluid Mechanics*, Vol. 350, 1997, p. 375–378. doi:[10.1017/S0022112097227291](https://doi.org/10.1017/S0022112097227291).
- [15] Spalart, P. R., “Detached-Eddy Simulation,” *Annual Review of Fluid Mechanics*, Vol. 41, No. 1, 2009, pp. 181–202. doi: [10.1146/annurev.fluid.010908.165130](https://doi.org/10.1146/annurev.fluid.010908.165130), URL <https://doi.org/10.1146/annurev.fluid.010908.165130>.
- [16] Menter, F., and Egorov, Y., “A Scale Adaptive Simulation Model using Two-Equation Models,” *43rd AIAA Aerospace Sciences Meeting and Exhibit, Aerospace Sciences Meetings*, Reno, NV, January 2005.

- [17] Travin, A., Shur, M., Strelets, M., and Spalart, P., “Detached-Eddy Simulations Past a Circular Cylinder,” *Flow, Turbulence and Combustion*, Vol. 63, No. 1, 2000, pp. 293–313. doi:10.1023/A:1009901401183, URL <https://doi.org/10.1023/A:1009901401183>.
- [18] Catalano, P., Wang, M., Iaccarino, G., and Moin, P., “Numerical simulation of the flow around a circular cylinder at high Reynolds numbers,” *International Journal of Heat and Fluid Flow*, Vol. 24, No. 4, 2003, pp. 463 – 469. doi:[https://doi.org/10.1016/S0142-727X\(03\)00061-4](https://doi.org/10.1016/S0142-727X(03)00061-4), URL <http://www.sciencedirect.com/science/article/pii/S0142727X03000614>, selected Papers from the Fifth International Conference on Engineering Turbulence Modelling and Measurements.
- [19] Zheng, W., Yan, C., Liu, H., and Luo, D., “Comparative assessment of SAS and DES turbulence modeling for massively separated flows,” *Acta Mechanica Sinica*, Vol. 32, No. 1, 2016, pp. 12–21.
- [20] Wang, S., Bell, J. R., Burton, D., Herbst, A. H., Sheridan, J., and Thompson, M. C., “The performance of different turbulence models (URANS, SAS and DES) for predicting high-speed train slipstream,” *Journal of Wind Engineering and Industrial Aerodynamics*, Vol. 165, 2017, pp. 46–57.
- [21] Squires, K. D., “Detached-Eddy Simulation: Current Status and Perspectives,” *Direct and Large-Eddy Simulation V*, edited by R. Friedrich, B. J. Geurts, and O. Métais, Springer Netherlands, Dordrecht, 2004, pp. 465–480.
- [22] Mockett, C., Greschner, B., Knacke, T., Perrin, R., Yan, J., and Thiele, F., “Demonstration of Improved DES Methods for Generic and Industrial Applications,” *Advances in Hybrid RANS-LES Modelling*, edited by S.-H. Peng and W. Haase, Springer Berlin Heidelberg, Berlin, Heidelberg, 2008, pp. 222–231.
- [23] Schwing, A. M., and Candler, G. V., “Detached-Eddy Simulation of Capsule Wake Flows and Comparison to ind-Tunnel Test Data,” *Journal of Spacecraft and Rockets*, Vol. 52, No. 2, 2015, pp. 439–449.
- [24] Forsythe, J. R., Squires, K. D., Wurtzler, K. E., and Spalart, P. R., “Detached-Eddy Simulation of the F-15E at High Alpha,” *Journal of Aircraft*, Vol. 41, No. 9, 2004, pp. 193–200.
- [25] Menter, F. R., and Kuntz, M., “Adaptation of Eddy-Viscosity Turbulence Models to Unsteady Separated Flow Behind Vehicles,” *The Aerodynamics of Heavy Vehicles: Trucks, Buses, and Trains*, edited by R. McCallen, F. Browand, and J. Ross, Springer Berlin Heidelberg, Berlin, Heidelberg, 2004, pp. 339–352.
- [26] Smith, C., Beratlis, N., Balaras, E., Squires, K., and Tsunoda, M., “Numerical investigation of the flow over a golf ball in the subcritical and supercritical regimes,” *International Journal of Heat and Fluid Flow*, Vol. 31, No. 3, 2010, pp. 262 – 273. doi: <https://doi.org/10.1016/j.ijheatfluidflow.2010.01.002>, URL <http://www.sciencedirect.com/science/article/pii/S0142727X10000147>, sixth International Symposium on Turbulence and Shear Flow Phenomena.
- [27] Cimarelli, A., Leonforte, A., and Angeli, D., “Direct numerical simulation of the flow around a rectangular cylinder at a moderately high Reynolds number,” *Journal of Wind Engineering and Industrial Aerodynamics*, Vol. 174, 2018, pp. 39 – 49. doi:<https://doi.org/10.1016/j.jweia.2017.12.020>, URL <http://www.sciencedirect.com/science/article/pii/S0167610517304622>.

- [28] Nakamura, Y., “Bluff-body aerodynamics and turbulence,” *Journal of Wind Engineering and Industrial Aerodynamics*, Vol. 49, No. 1, 1993, pp. 65 – 78. doi:[https://doi.org/10.1016/0167-6105\(93\)90006-A](https://doi.org/10.1016/0167-6105(93)90006-A), URL <http://www.sciencedirect.com/science/article/pii/016761059390006A>.